LBNL-49331

# Numerical Simulation of Premixed Turbulent Methane Combustion

John B. Bell, Marcus S. Day and Joseph F. Grcar
Computing Sciences Directorate
Lawrence Berkeley National Laboratory
Berkeley, California 94720

This work was supported under the SciDAC Program by the Director, Office of Science, Office of Advanced Scientific Computing Research, Mathematical, Information, and Computational Sciences Division of the U.S. Department of Energy, contract No. DE-AC03-76SF00098.

**Numerical Simulation of Premixed Turbulent Methane Combustion**

**Abstract**

In this paper we study the behavior of a premixed turbulent methane flame in three dimensions using numerical simulation. The simulations are performed using an adaptive time-dependent low Mach number combustion algorithm based on a second-order projection formulation that conserves both species mass and total enthalpy. The species and enthalpy equations are treated using an operator-split approach that incorporates stiff integration techniques for modeling detailed chemical kinetics. The methodology also incorporates a mixture model for differential diffusion. For the simulations presented here, methane chemistry and transport are modeled using the DRM-19 (19-species, 84-reaction) mechanism derived from the GRIMech-1.2 mechanism along with its associated thermodynamics and transport databases. We consider a lean flame with equivalence ratio 0.8 for two different levels of turbulent intensity. For each case we examine the basic structure of the flame including turbulent flame speed and flame surface area. The results indicate that flame wrinkling is the dominant factor leading to the increased turbulent flame speed. Joint probability distributions are computed to establish a correlation between heat release and curvature. We also investigate the effect of turbulent flame interaction on the flame chemistry. We identify specific flame intermediates that are sensitive to turbulence and explore various correlations between these species and local flame curvature. We identify different mechanisms by which turbulence modulates the chemistry of the flame.

# Introduction

Turbulence affects the process of combustion through a wide variety of mechanisms. Traditional approaches, based on asymptotic analysis, show that velocity-induced tangential strain at the flame surface can dramatically enhance or suppress combustion activity in the flame zone depending on Lewis number. These effects have been studied using results from steady flat-flame counterflow experiments (see [1–5]). As discussed in the review by Peters [6], this type of information can readily be incorporated into engineering models through the flamelet concept.

In recent years there have been a number of studies aimed toward elucidating key mechanisms in premixed turbulent combustion using numerical simulation with detailed kinetics mechanisms. Many of these studies have focused on the interaction of a single vortical structure with a laminar premixed flame. Such studies typically consider either a planar vortex pair (for example, see [7–11]), or an axisymmetric toroidal vortex (for example, see [12–19]).

In two dimensions, Baum et al. [20] studied turbulent flame interactions for detailed hydrogen chemistry, and Haworth et al. [21] have examined the effect of inhomogeneous reactants for propane–air flames used detailed propane chemistry. More recently Tanahashi et al. [22] have performed direct numerical simulations of turbulent, premixed hydrogen flames in three dimensions with detailed hydrogen chemistry.

In this paper we investigate the behavior of premixed turbulent methane flames in three dimensions using numerical simulations. The computational setting is similar to the configuration used by Trouve and Poinsot [23] and by Zhang and Rutland [24] for single step chemistry and by Tanahashi et al. [22] for comprehensive hydrogen chemistry. We begin with a flat flame initialized using the laminar flame solution. A field of isoptropic decaying turbulence is superimposed over the incoming fuel stream. The flame deflects in response to the turbulent structures. We present two scenarios, representing different levels of turbulent intensity in the fuel stream. Analysis includes computation of an effective turbulent flame speed, flame surface area, and scatter plots to characterize the deviation of the flame from the laminar flame solution.

# Numerical Model

Our computational approach uses a hierarchical adaptive mesh refinement (AMR) algorithm based on an approximate projection formulation for incompressible flow by Almgren et al. [25], subsequently extended to low Mach number combustion by Pember et al. [26]. The methodology was extended to model detailed kinetics and differential diffusion by Day and Bell [27]. Here we sketch the model and numerical implementation below; the reader is referred to [27] for details.

We consider a gaseous mixture, ignoring Soret and Dufour effects, body forces and radiative heat transfer, and assume a mixture model for species diffusion [28, 29]. For an unconfined domain, we have

$$\frac{\partial \rho U}{\partial t} + \nabla \cdot \rho U U = -\nabla \pi + \nabla \cdot \tau, \tag{1}$$

$$\frac{\partial \rho Y_m}{\partial t} + \nabla \cdot U \rho Y_m = \nabla \cdot \rho \mathcal{D}_m \nabla Y_m + \dot{\omega}_m, \tag{2}$$

$$\frac{\partial \rho h}{\partial t} + \nabla \cdot U \rho h = \nabla \cdot \frac{\lambda}{c_{p,mix}} \nabla h + \sum_m \nabla \cdot h_m (\rho \mathcal{D}_m - \frac{\lambda}{c_{p,mix}}) \nabla Y_m \tag{3}$$

where $\rho$ is the density, $U$ is the velocity, $\pi$ is the pressure variation from a uniform ambient pressure, $Y_m$ is the mass fraction of species $m$, $h$ is the mass-weighted enthalpy of the gas mixture, $T$ is the temperature, and $\dot{\omega}_m$ is the net production rate for $\rho Y_m$ due to chemical reactions. Also, $\lambda$ is the thermal conductivity, $\tau$ is the stress tensor, $c_{p,mix}$ is the specific heat of the mixture and $h_m(T)$ and $\mathcal{D}_m$ are the enthalpy and species mixture-averaged diffusion coefficients of species $m$, respectively.

These evolution equations are supplemented by an equation of state for a perfect gas mixture:

$$p_0 = \rho R_{mix} T = \rho \mathcal{R} T \sum_m \frac{Y_m}{W_m} \tag{4}$$

where $W_m$ is the molecular weight of species $m$.

In the low Mach number limit, the thermodynamic pressure given by equation (4) remains approximately constant as the flow evolves. Differentiating the equation of state in the frame of the fluid, and using the conservation equations to replace advective derivatives, we obtain an elliptic constraint on the evolving velocity field:

$$\begin{aligned} \nabla \cdot U &= \frac{1}{\rho c_p T} \left( \nabla \cdot \lambda \nabla T + \sum_m \rho \mathcal{D}_m \nabla Y_m \cdot \nabla h_m \right) + \\ &+ \frac{1}{\rho} \sum_m \frac{W}{W_m} \nabla \cdot \rho \mathcal{D}_m \nabla Y_m \; + \frac{1}{\rho} \sum_m \left( \frac{W}{W_m} - \frac{h_m(T)}{c_{p,mix} T} \right) \dot{\omega}_m \equiv S \end{aligned} \tag{5}$$

where $W = (\sum_m Y_m / W_m)^{-1}$ and $c_{p,mix} = \sum_m Y_m dh_m/dT$.

The single-grid scheme that forms the basis for our adaptive algorithm combines a symmetric operator-split coupling of chemistry and diffusion processes with a projection method for incorporating the velocity divergence constraint. First, equations (1–3) are advanced in time using a second-order Godunov scheme for advective terms and a time-centered Crank-Nicolson discretization for diffusion. Because the transport coefficients depend on both temperature and composition, we adopt a sequential, predictor-corrector scheme to guarantee second-order treatment of nonlinear diffusion effects. The chemistry is advanced using time-implicit backward differentiation methods in VODE [30]. The implicit diffusion and chemistry components of the algorithm are time-split symmetrically to ensure that the composite algorithm remains second-order. The velocity field resulting from the advection/diffusion/chemistry step is then decomposed using a density-weighted approximate projection. The component satisfying the constraint, equation (5), updates the velocity field, and the remainder updates the perturbational pressure. The Godunov advection scheme is explicit consequently the time step is limited by a CFL restriction. Since the advective time scale is typically larger than the fastest time scales associated with the chemical kinetics, this does not appear to be a serious disadvantage for time dependent simulations.

The extension of the above algorithm to adaptive mesh refinement is based on a hierarchical refinement strategy. Our methodology uses a system of overlaid grids with successively finer spacing in time and space. Fine grids are formed by uniformly dividing coarse cells in each direction. Increasingly finer levels, each consisting of a union of rectangular grid patches, overlay coarser grid levels until the solution is adequately resolved. An error estimation procedure identifies where refinement is needed and grid generation procedures dynamically create or remove rectangular fine grid patches as requirements change.

The complete adaptive algorithm has a number of desireable properties. The overall method is second-order accurate in space and time, and discretely conserves species mass and enthalpy. Furthermore, the algorithm satisfies a free-stream preservation property guaranteeing that nonreacting isothermal flow remains numerically isothermal during species transport. The parallel implementation of this methodology for distributed memory parallel processors is discussed by Bell, et al. [31].

# Results

Simulations are performed in a computational domain that measures 8×8×16 mm as illustrated in Fig. 1. We used DRM-19 [32] for the chemistry mechanism, thermodynamics and transport database. The flame is initialized with a steady flat methane flame solution at equivalence ratio $\phi = 0.8$. The inflow boundary conditions for the velocity fields are given as $\vec{u}(\vec{x},t) = 1.5\ S_L\hat{z} + \vec{u}'(\vec{x},t)$, where $S_L$ is the laminar flame speed. The turbulent perturbations $\vec{u}'(\vec{x},t)$ are taken from an auxiliary calculation, and represent decaying isotropic turbulence in the inflow stream, computed over a triply-periodic 8×8×8 mm domain. The initial field is generated with random phase, and then allowed to evolve until realistic phases are established. The resulting field was converted to time-dependent inflow boundary conditions using Taylor's hypothesis. Perturbations in velocity are extended into the domain from the inflow boundary, and are damped to zero 1 mm from the flame surface.

The domain is discretized at the coarsest level using a 32×32×64 grid. Two additional refinement levels are superimposed over successively smaller portions of the domain, each a factor of two finer, and fully contained within its parent coarser grid. All three refinement levels span the distance from inflow to past the flame surface to ensure adequate resolution of both the flame and the incoming velocity fluctuations. Typically, simulations required approximately 750 hours of wall-clock time using 64-96 processesors of an IBM SP3.

For the domain considered here, the Reynolds number based on the laminar flame thickness, flame speed and viscosity of the the fuel is approximately 2100. Consequently, as the turbulent fluctuations enter the domain they continue to decay as they propagate toward the flame. As a result by using two different initial altitudes for the flame we are able to investigate two different turbulent intensities within the same problem configuration. In the first case, the flame is initialized at $z$=8mm (based on the peak value of heat release). For this case, the flame encounters an upstream turbulence intensity of approximately .45 m/s ($\approx 1.7S_L$). In the second case, the flame is initialized at $z$=4mm, where the upstream turbulence intensity is approximately 1.1 m/s ($\approx 4.3S_L$). For these cases, the integral scale is approximately 0.1 cm. and the flame thickness as defined by $(T_b - T_u)/\max(|\nabla T|)$ is 0.0525 cm. We will refer to these cases as the weak and strong cases, respectively.

In Fig. 2, we show volume rendered images of the heat release that represent the overall flame surface. As expected, stronger turbulence leads to increased wrinkling of the flame. To quantify this notion, we observe that the peak heat release for this flame correlates with a temperature of approximately 1500K. We then approximate the flame surface area by the area of the $T = 1500$ isosurface. For the weak and strong cases we obtain $1.23A_L$ and $1.64A_L$, respectively, where $A_L$ is the flame surface area for the corresponding flat laminar flame.

For the case considered here we can compute the net consumption rate of $CH_4$ integrated over the computational domain. The fuel consumption rate, suitably scaled, gives the turbulent flame speed. For the weak and strong cases, we obtain $S_T = 1.35\ S_L$ and $S_T = 1.85\ S_L$, respectively. Comparing these speeds to the increases in flame area we see that the dominant factor in enhancing the flame speed is the increase in flame surface area associated with the wrinkling of the flame. There is, however, substantial variation in flame intensity across the flame surface. To quantify this variation, we compute the joint probability distribution function of heat release and mean curvature, $\kappa$ of the flame surface with the convention that positive curvature means the flame is concave toward the unburnt fuel. In Fig. 3 we show the joint PDF's for the weak and strong turbulence cases. The two PDF's are quite similar, with the stronger turbulence showing a greater variation in curvature. Both images show a strong correlation between heat release and curvature. Tanahasi et al. [22] found a similar result for hydrogen flames.

We now turn our attention to a more detailed examination of the behavior of the chemistry within the flame. By integrating the chemical production terms over the domain we can compute an overall carbon reaction network for the aggregate chemistry of the flame. The resulting carbon reaction path diagram, depicted in Fig. 4 for the strong turbulence case, shows little difference compared to the laminar flame. As a first step toward analyzing the local effect of turbulence on chemistry, we compute scatter plots of species mole fraction versus temperature and compare the result to the laminar flame solution parameterized by temperature. For the combination of turbulent intensity, integral scale and equivalence ratio considered here, most of the species mole fractions remain tightly clustered around the laminar flame solution. Fig. 5a, which shows the mole fraction of HCO versus $T$, is typical of most other species. In Fig. 5b, we show a scatter plot of the HCO mole fraction versus total heat release, $Q$. The figure shows two branches with the lower branch corresponding to the cold side of the flame and the upper branch corresponding to the hot side of the flame. The correlation between peak heat release and HCO indicates that HCO is a good flame marker for these flames as was oberved by Najm et al. [8] for vortex flame interaction.

There are four species, $HO_2$, $H_2$, $CH_3O$ and $C_2H_4$, that show substantial variation in mole fraction compared to the laminar flame solution. Scatter plots for these four species are presented in Fig. 6. For each species the variability increases with

increasing turbulent intensity. We note also that the variability arises primarily on the cold side of the flame. Above 1500 degrees the mole fractions of these species also cluster around the laminar flame solution.

In Fig. 7 we show typical vertical slices of the $CH_3O$ and $C_2H_4$ mole fractions from the strong turbulence case. For strong positive curvature we see an abundance of $CH_3O$ and an absence of $C_2H_4$ with the opposite occuring in regions of strong negative curvature. This point is further illustrated by the joint PDF's of the $CH_3O$ and $C_2H_4$ mole fractions versus $\kappa$ shown in Fig. 8. $CH_3O$, which is enhanced in regions of positive curvature, is created primarily from reaction of $CH_3$ and $HO_2$. Both of these species correlate with positive curvature and we observe a dramatic increase in the intensity of $CH_3O$ production in regions of positive curvature. The mechanism for enhanced $C_2H_4$ in regions of negative curvature is quite different. There, rather than observing a change in the intensity of the reactions, we observe that the regions of production and destruction broaden and separate in regions of negative curvature. This spatial separation leads to an increased lifetime for $C_2H_4$ molecules resulting a higher mole fraction in regions negative curvature. The behavior of these two species illustrate two distinct mechanisms by which turbulence modulates flame chemistry.

# Conclusions

In this paper we have used numerical simulations with detailed chemistry to study the behavior of turbulent, premixed methane combustion in three space dimensions. Two cases, corresponding varying levels of turbulent intensity, show increased flame area and enhancements of the laminar flame speed by 35% and 85%. The basic flame structure exhibits a correlation between heat release and curvature. We also show similar correlations between some of the flame intermediaries and curvature illustrating the local variability of the chemistry. A more detailed analysis reveals two distinct scenarios leading to curvature dependence illustrating the different mechanisms by which turbulence modulates the flame.

# References

[1] F. Egolfopoulos. Dynamics and structure of unsteady, strained, laminar premixed flames. *Proc. Combust. Inst.*, 25:1365–1373, 1994.

[2] R. J. Kee, J. A. Miller, G. H. Evans, and G. Dixon-Lewis. A computational model of the structure and extinction of strained, opposed flow premixed methane-air flames. *Proc. Combust. Inst.*, 22:1479–1494, 1988.

[3] C. K. Law. Dynamics of stretched flames. *Proc. Combust. Inst.*, 22:1381–1402, 1988.

[4] C. Petrov and A. Ghoniem. The transient response of strained laminar-premixed flames. *Combust. Flame*, 102:401–417, 1995.

[5] B. Rogg. Response and flamelet structure of stretched premixed methane-air flames. *Combust. Flame*, 73:45–46, 1988.

[6] N. Peters. Laminar flamelet concepts in turbulent combustion. *Proc. Combust. Inst.*, 21:1231–1250, 1986.

[7] H. N. Najm and P. S. Wyckoff. Premixed flame response to unsteady strain rate and curvature. *Combust. Flame*, 110(1-2):92–112, 1997.

[8] H. N. Najm, O. M.. Knio, P. P. Paul, and P. S. Wyckoff. A study of flame observables in premixed methane-air flames. *Combust. Sci. Technol.*, 140:369–403, 1998.

[9] H. N. Najm, P. P. Paul, C. J. Mueller, and P. S. Wyckoff. On the adequacy of certain experimental observables as measurements of flame burning rate. *Combust. Flame*, 113(3):312–332, 1998.

[10] T. Mantel and J.-M. Samaniego. Fundamental mechanisms in premixed turbulent flame propagation via flame-vortex interactions Part II: Numerical simulation. *Combust. Flame*, 118:557–582, 1999.

[11] J. B. Bell, N. J. Brown, M. S. Day, M. Frenklach, J. F. Grcar, and S. R. Tonse. The dependence of chemistry on the inlet equivalence ratio in vortex-flame interactions. *Proc. Combust. Inst.*, 28:1933–1939, 2000.

[12] J. F. Driscoll, D. J. Sutkus, W. L. Roberts, M. E. Post, and L. P. Goss. The strain exerted by a vortex on a flame - determined from velocity field images. *Combust. Sci. Technol.*, 96:213–229, 1996.

[13] C. J. Mueller, J. F. Driscoll, D. L. Reuss, and M. C. Drake. Effect of unsteady stretch on the strength of a freely-propagating flame wrinkled by a vortex. *Proc. Combust. Inst.*, 26:347–355, 1996.

[14] C. J. Mueller, J. F. Driscoll, D. L. Reuss, M. C. Drake, and Martin E. Rosalik. Vorticity generation and attenuation as vortices convect through a premixed flame. *Combust. Flame*, 112(3):342–358, 1998.

[15] C. J. Mueller, J. F. Driscoll, D. J. Sutkus, W. L. Roberts, M. C. Drake, and M. D. Smooke. Effects of unsteady stretch rate on OH chemistry during a flame-vortex interaction: To assess flamelet models. *Combust. Flame*, 100:323–331, 1995.

[16] W. L. Roberts and J. F. Driscoll. A laminar vortex interacting with a premixed flame: Measured formation of pockets of reactants. *Combust. Flame*, 87:245–256, 1991.

[17] W. L. Roberts, J. F. Driscoll, M. C. Drake, and L. P. Goss. Images of the quenching of a flame by a vortex — To quantify regimes of turbulent combustion. *Combust. Flame*, 98:58–69, 1993.

[18] W. L. Roberts, J. F. Driscoll, M. C. Drake, and J. W. Ratcliffe. OH fluorescence images of the quenching of a premixed flame during an interaction with a vortex. *Proc. Combust. Inst.*, 24:169, 1992.

[19] J. C. Rolon, F. Aguerre, and S. Candel. Experiments on the interaction between a vortex and a strained diffusion flame. *Combust. Flame*, 100(3):422–429, 1995.

[20] M. Baum, T. J. Poinsot, D. C. Haworth, and N. Darabiha. Direct numerical simulation of $H_2/O_2/N_2$ flames with complex chemistry in two-dimensional turbulent flows. *J. Fluid Mech.*, 281:1–32, 1994.

[21] D. C. Haworth, R. J. Blint, B. Cuenot, and T. J. Poinsot. Numerical simulation of turbulent propane-air combustion with nonhomogeneous reactants. *Combust. Flame*, 121:395–417, 2000.

[22] M. Tanahasi, M. Fujimura, and T. Miyauchi. Coherent fine scale eddies in turbulent premixed flames. *Proc. Combust. Inst.*, 28:529–535, 1998.

[23] A. Trouve and T. Poinsot. The evolution equation for the flame surface density in turbulent premixed combustion. *J. Fluid Mech.*, 278:1–31, 1994.

[24] S. Zhang and C. J. Rutland. Premixed flame effects on turbulence and pressure-related terms. *Combust. Flame*, 102:447–461, 1995.

[25] A. S. Almgren, J. B. Bell, P. Colella, L. H. Howell, and M. Welcome. A conservative adaptive projection method for the variable density incompressible Navier-Stokes equations. *J. Comput. Phys.*, 142:1–46, 1998.

[26] R. B. Pember, L. H. Howell, J. B. Bell, P. Colella, W. Y. Crutchfield, W. A. Fiveland, and J. P. Jessee. An adaptive projection method for unsteady, low-Mach number combustion. *Comb. Sci. Technol.*, 140:123–168, 1998.

[27] M. S. Day and J. B. Bell. Numerical simulation of laminar reacting flows with complex chemistry. *Combust. Theory Modelling*, 4(4):535–556, 2000.

[28] R. J. Kee, G. Dixon-Lewis, J. Warnatz, M. E. Coltrin, and J. A. Miler. A FORTRAN computer code package for the evaluation of gas-phase multicomponent transport properties. Sandia Technical Report SAND86-8246, Sandia National Laboratories, 1986.

[29] J. Warnatz. Influence of transport models and boundary conditions on flame structure. In N. Peters and J. Warnatz, editors, *Numerical methods in flame propagation*. Friedr. Viewweg and Sohn, Wiesbaden, 1982.

[30] P. N. Brown, G. D. Byrne, and A. C. Hindmarsh. VODE: A variable coefficient ode solver. *SIAM J. Sci. Stat. Comput.*, 10:1038–1051, 1989.

[31] J. B. Bell, M. S. Day, A. S. Almgren, M. J. Lijewski, and C. A. Rendleman. A parallel adaptive projection method for low mach number flows. In M. J. Baines, editor, *Numerical Methods for Fluid Dynamics VII*, pages 207–213, Oxford and Reading Universities, March 2001. ICFD. *also to appear in Int. J. Num. Meth. Fluids*.

[32] A. Kazakov and M. Frenklach. Reduced reaction sets based on GRI-Mech 1.2. `http://www.me.berkeley.edu/drm/`.

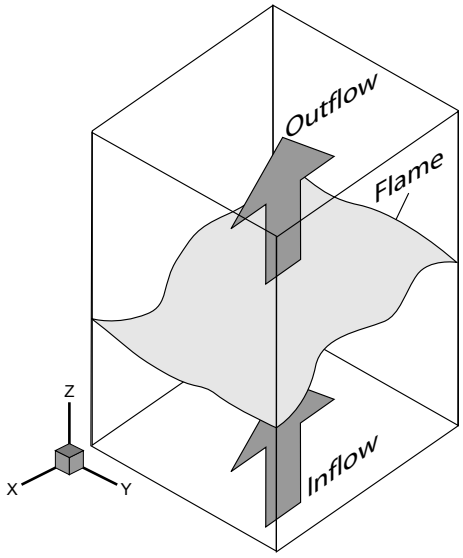


Figure 1: *Schematic of the computational domain. Periodic boundary conditions are enforced on the sides of the domain. Unburnt fuel and oxidizer enter the domain at the bottom and combustion products exit at the top.*

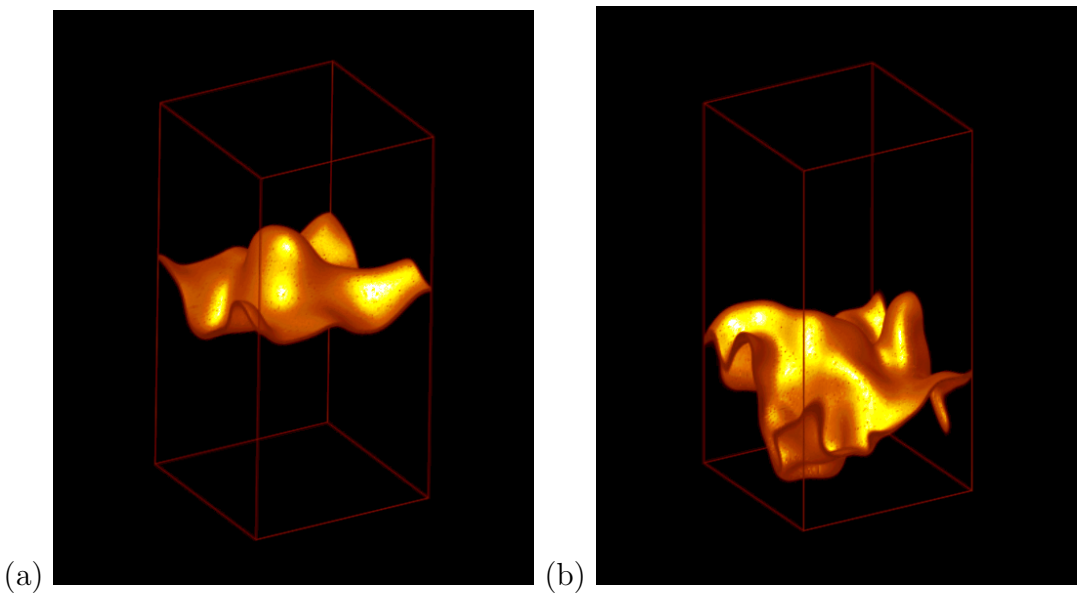

(a) (b)

Figure 2: *Volume rendered image showing surface of maximum heat release for the weak (a) and strong (b) turbulence cases.*

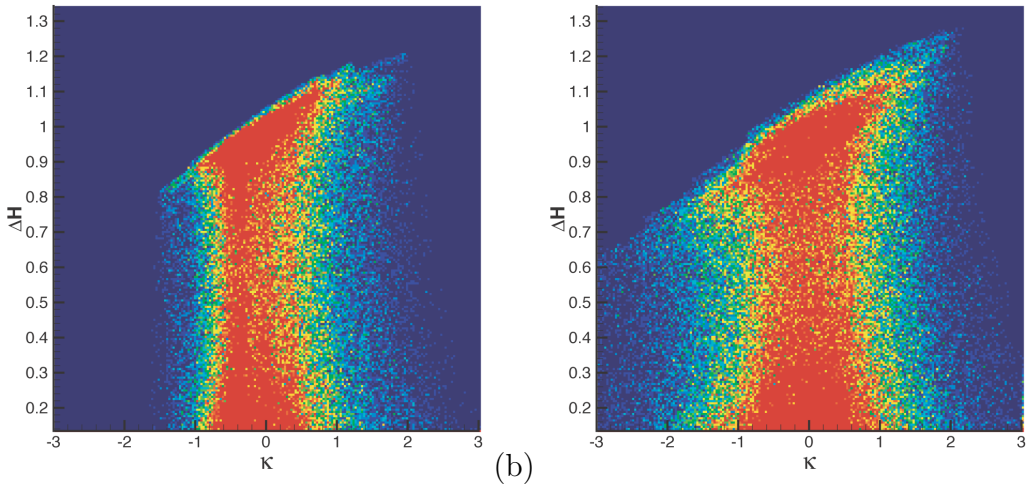


(a) (b)

Figure 3: *Joint probability distribution of heat release and mean curvature. The color scale is a standard rainbow palette with dark blue corresponding to zero probability and red indicating probabilities greater than* $2.5 \times 10^{-6}$*. The heat release is scaled by the peak value attained by the initial flat laminar flame, and the curvature is scaled by the inverse of the flat flame thickness. Here, (a) is the weak turbulence case and (b) is the strong case.*

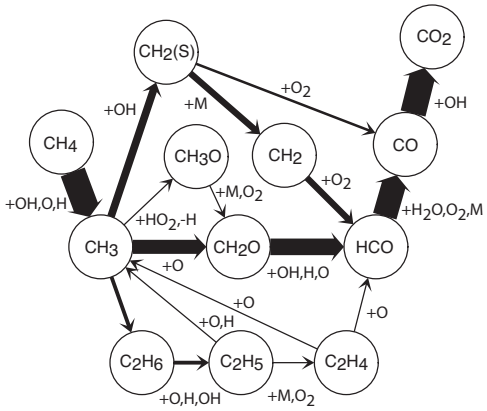


Figure 4: *Carbon reaction path diagram for the strong turbulence case. The thickness of the arrows indicates the relative amount of carbon reacting along the given pathway. The edge labels indicate the reaction partners participating in the reaction.*

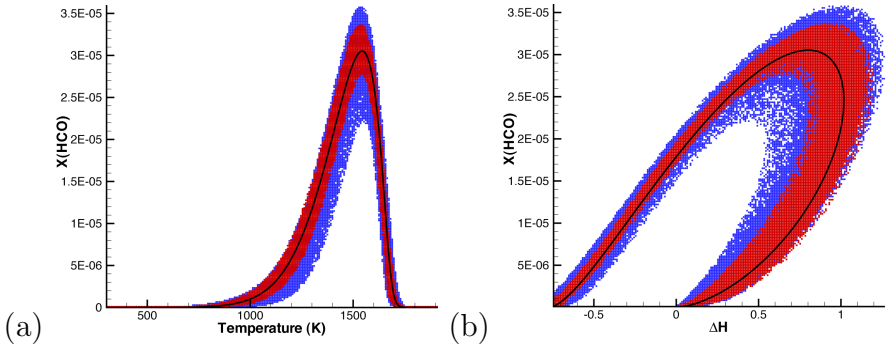


Figure 5: *(a) Scatter plot of the HCO mole fraction vs. T. The black curve is the laminar flame solution. (b) Scatter plot of the HCO mole fraction vs. $\Delta H$. The blue dots are for strong turbulence and the overlayed red dots are for weak turbulence.*

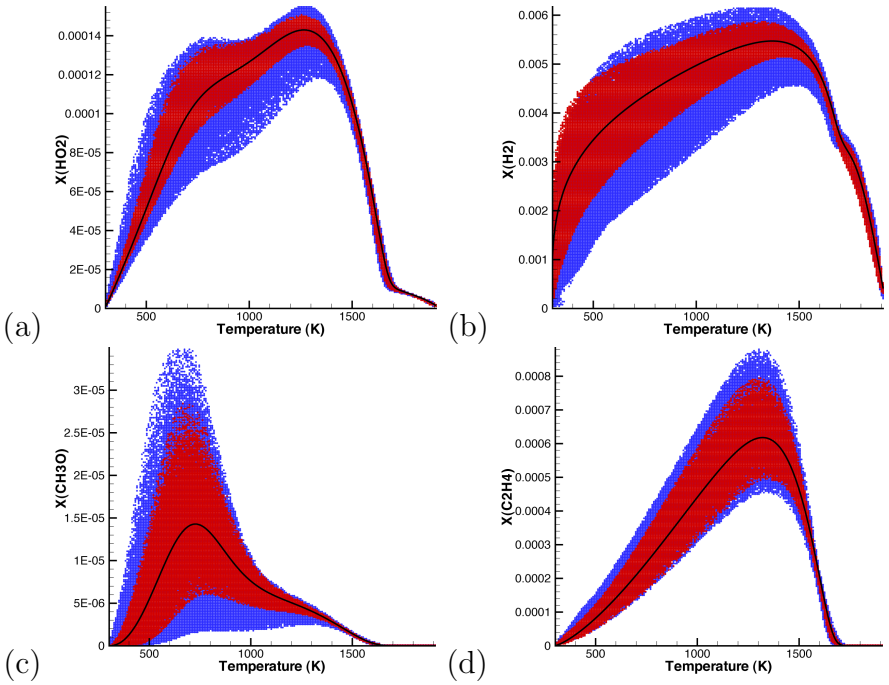


Figure 6: *Scatter plots of mole fraction of (a) $HO_2$, (b) $H_2$, (c) $CH_3O$, and (d) $C_2H_4$ versus $T$.*

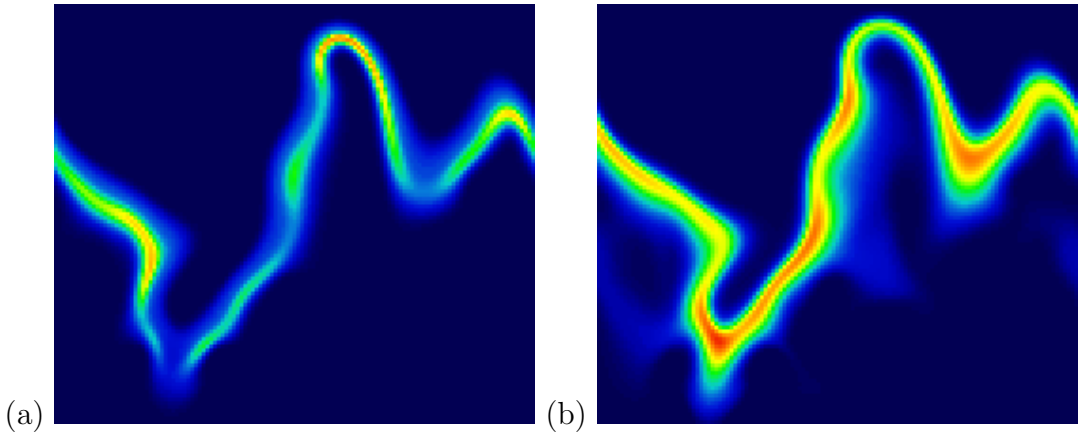


Figure 7: *Vertical slices from strong turbulence case showing mole fractions of (a) $CH_3O$ and (b) $C_2H_4$ using a rainbow color palette.*

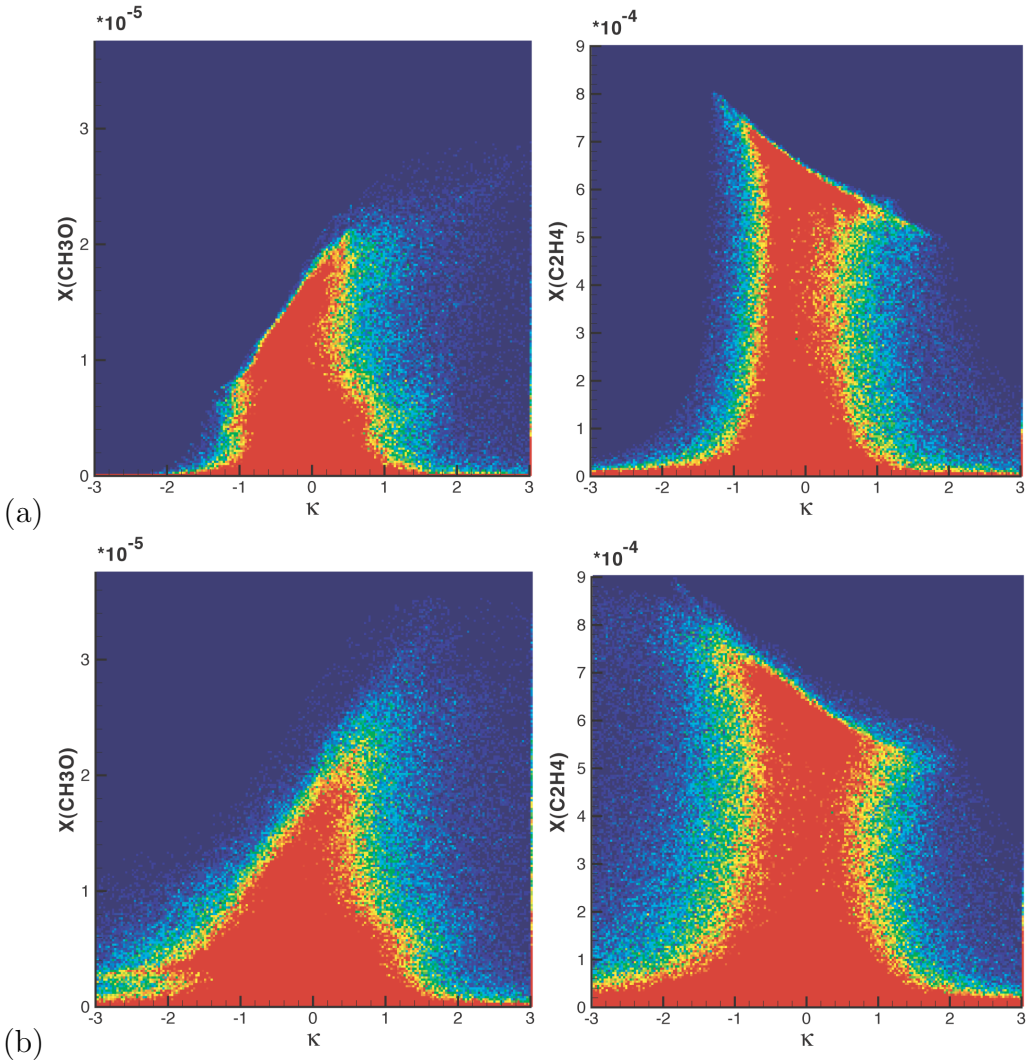


Figure 8: *Joint probability distributions for $CH_3O$ and $C_2H_4$ vs. $\kappa$ for both the (a) weak and (b) strong turbulence cases. Here, the values are scaled so that red corresponds to probabilities greater than* $5. \times 10^{-6}$.